Structural and Chemical State of Doped and Impregnated Mesoporous Ni/CeO_2 Catalysts for the Water-gas Shift

Dimitriy Vovchok [a, b], Curtis J. Guild [c], Jordi Llorca [d], Robert Palomino [a], Iradwikanari Waluyo [e], José A. Rodriguez [a, b], Steven L. Suib, [c,] Sanjaya D. Senanayake [b, *]*

[a] Department of Chemistry, Stony Brook University, Stony Brook, NY, 11794 USA

[b] Chemistry Department, Brookhaven National Laboratory, Upton, NY, 11973 USA

[c] Department of Chemistry, University of Connecticut, 55 N. Eagleville Rd., Storrs, CT 06269 USA

[d] Institute of Energy Technologies, Department of Chemical Engineering and Barcelona Research Center in Multiscale Science and Engineering. Technical University of Catalonia. Barcelona 08019, Spain

[e] National Synchrotron Light Source II. Brookhaven National Laboratory, Upton, NY, 11973 USA

[*] Corresponding author: Bldg. 555A, Brookhaven National Lab, P.O. Box 5000, Upton, NY 11973-5000, 631-344-4343, Steven.suib@uconn.edu ; ssenanay@bnl.gov

1. Abstract

Mesoporous Ni/CeO_2 catalysts of variable loadings were prepared using in-situ doping and impregnation synthesis techniques. The catalysts were found to exhibit activity for the water-gas shift (WGS) reaction, particularly at temperatures above 250°C. Structural, electronic, and surface chemical characterizations of the materials were carried out using in-situ X-ray diffraction (XRD), in-situ X-ray absorption (XANES), and in-situ infrared (DRIFTS) techniques. The effects of metal loading and preparation method on these properties were closely studied in order to develop a more complete understanding of the design and application of metal-loaded mesoporous CeO_2 catalysts. For WGS reaction activity, the in-situ doping method was observed to be superior, and overall activity was observed to increase with increasing metal loadings. Simple normalization of activity data to nominal nickel content revealed a trend favoring lower loadings, indicating higher activity per unit nickel. Structural properties and surface chemistry were observed to depend both on metal loading and preparation method. Nickel loadings as low as 1 wt% prepared by in-situ doping were found to display the most favorable metal-support interactions for the WGS reaction.

2. Introduction

The use of ceria-supported metal catalysts has been well established for the water-gas shift (WGS) reaction. In previous studies, we have explored the novel mesoporous CeO_2 platform as an active support material for metal-free and metal-loaded WGS catalysts[1]. We have also introduced copper to the mesoporous CeO_2 system, resulting in highly active WGS catalysts that exhibit strong surface metal-support interactions[2].

While copper remains the mainstream metal of choice for development of WGS catalysts[3], other transition metals such as nickel have also been explored. While nickel is typically used in reactions such as CO_2 methanation[4, 5] and CO_2 reforming of methane[6, 7], this species has also been used in supported catalysts for the WGS reaction[8-10], as well as the reverse WGS reaction[11]. Ni/CeO_2 catalysts in particular were found to be particularly active for the high temperature stage of the WGS reaction (HT-WGS)[12]. Typically, the activity of Ni/CeO_2 catalysts is enhanced by the use of additives such as sodium[13] or by utilizing alloys such as Ni-Cu[12], although standalone Ni/CeO_2 catalysts were reported as well[10].

In this study, we continue our evaluation of mesoporous CeO_2 based materials by synthesizing an array of mesoporous Ni/CeO_2 catalysts. In previous studies, the preparation method of Ni/CeO_2 catalysts was suggested to have an impact on catalytic properties[11]. We have therefore synthesized our materials using two preparation methods: in-situ doping and wet impregnation. With each preparation method, we have synthesized catalysts with variable nickel loadings. The purpose of this research was to evaluate the effect of preparation method and nickel loading on the activity, structure, and surface chemistry of the mesoporous Ni/CeO_2 catalysts.

3. Experimental

3.1. Catalyst Synthesis

To prepare in-situ doped catalysts, the procedure from section 2.3.1. was used, with the addition of nickel precursor. Pluronic P-123 was heated in an oven to 60°C. 3g of the P-123 was dissolved in 15 mL 2-butanol under gentle heating and stirring. 8.7g of $Ce(NO_3)_3*6H_2O$ was added, along with variable amounts of amount Ni(II) salt and 1.5mL HNO_3. Heat was applied for 1 hour to dissolve all materials into a single phase. The materials were dried in an oven at 120°C for 4 hours, then washed three times with ethanol. The in-situ doped catalysts **d-1NiCe**, **d-5NiCe**, and **d-10NiCe** were produced using this method.

To prepare the impregnated catalysts, the procedure from section 2.3.1. was used to prepare mesoporous CeO_2 first, without calcination. 10 mL solutions of 1, 5, and 10 mmol/L Ni^{2+} salt in ethanol were each added to 100 mg of the uncalcined mesoporous CeO_2. The solutions were stirred to equilibrium for 12 hours. The product was centrifuged and washed three times with ethanol. Calcination was carried out at 450°C for 4 hours. The impregnated catalysts **i-1NiCe**, **i-5NiCe**, and **i-10NiCe** were produced using this method. The maximum nickel contents of the **i-1NiCe**, **i-5NiCe**, and **i-10NiCe catalysts** are 0.6, 2.9, and 5.5 wt%, respectively.

It is important to note that the in-situ doped and impregnated catalysts are *not directly comparable in terms of their labels and loadings.* E.g., **d-5NiCe** contains up to 5 wt% Ni, whereas **i-5NiCe** only contains up to 2.9 wt% Ni. Exact evaluations of Ni content were not performed.

3.2. Transmission Electron Microscopy

Microstructural characterization by high resolution transmission electron microscopy (HRTEM) was performed at 200 kV in a JEOL 2010F microscope equipped with a field emission source. The point-to-point resolution of the electron microscope was 0.19 nm, and the resolution between lines was 0.14 nm. For scanning transmission electron microscopy, high angle annular dark field, and energy-dispersive X-ray spectroscopy (STEM-HAADF-EDX) characterization, the instrument used was a Tecnai G^2 F20 S-TWIN microscope equipped with a field emission electron source and operated at 200 kV. HRTEM analyses were carried out for the **d-5NiCe** and **i-5NiCe** samples.

3.3. X-ray Photoelectron Spectroscopy

A Ce 4d + Ni 3s XPS spectrum measured for **d-5NiCe** was included in this study. This spectrum was collected at beamline U12 at the National Synchrotron Light Source (NSLS) at Brookhaven National Laboratory.

3.4. In-situ X-ray Diffraction (XRD)

In-situ X-ray Diffraction (XRD) experiments detailed in this study were performed at Advanced Photon Source (APS) in Argonne National Laboratory at beamline 17BM-B. The experiments were carried out using the Clausen[14] capillary flow reactor in typical configuration (see section 2.3.5). The WGS reactant gas (5% CO, 3% H_2O, balance He) was flown at a rate of 10 cc/min. The temperature profile for the experiments consisted of stepwise heating and cooling up to 400°C in 50°C increments. X-ray Diffraction patterns are collected continuously during the experiment. Outflow gas during XRD experiments was analyzed using a Residual Gas Analyzer (RGA) quadrupole mass spectrometry unit in order to provide a qualitative WGS activity analysis by monitoring the production of CO_2 gas. The X-ray

wavelength utilized for the XRD experiments was 0.45336 Å. X-ray Diffraction patterns were plotted in Origin and processed using the GSAS II software[15] to obtain structural information via Rietveld refinement[16].

3.5. X-ray Absorption Spectroscopy (XAS: NEXAFS and in-situ XANES)

Ex-situ soft X-ray near-edge X-ray absorption spectroscopy (NEXAFS) measurements were collected in total electron yield (TEY) mode at beamline 23-ID-2 (IOS) at the National Synchrotron Light Source II (NSLS-II). The Ce $M_{4,5}$-edge, Ni $L_{2,3}$-edge, and O K-edge measurements were collection for the **d-5NiCe** and **d-10NiCe** samples.

The in-situ Ni K-edge XANES experiment detailed in this study was performed at the Advanced Photon Source (APS) in Argonne National Laboratory at beamline 20BM-B. The Clausen[14] reactor cell was used. The sample was pretreated in helium flow at 200°C for 2 hours and cooled to room temperature. WGS reactant gas (5% CO, 3% H_2O, balance He) was then flown at a rate of 10 cc/min. The temperature profile of the in-situ XANES experiment consisted of temperature steps of 25, 100, 150, 250, 350, and 450°C. This experiment was only performed for the **i-5NiCe** sample. All X-ray absorption spectra were processed using the Athena software[17], which includes plotting, normalization, and basic principal component analysis.

3.6. In-situ Diffuse Reflectance Infrared Fourier Transform Spectroscopy (DRIFTS)

DRIFTS experiments were performed at Brookhaven National Laboratory. The Harrick reactor cell was loaded with sample material and heated to 200°C under helium, remaining for between 2 and 18 hours. Infrared spectra (4000 to 800 cm^{-1}) were recorded every 85 seconds. The sample was cooled to room temperature and WGS reactants (5% CO, 3% H_2O in He) were introduced into the cell. The cell was then heated to 100°C and then to 400°C in 50°C

increments, remaining at each temperature for approximately 30 minutes while collecting infrared spectra. KBr background was subtracted from all spectra. Data were processed using Thermo Scientific OMNIC 8 software. DRIFTS experiments were only carried out for **d-5NiCe** and **i-5NiCe** samples.

4. Results and Discussion

4.1. Imaging

HRTEM analysis was performed on the **d-5NiCe** and **i-5NiCe** samples. Representative images obtained for both catalysts are presented in Figure 1. Analysis of the **i-5NiCe** material (Figure 1b) revealed a monodisperse distribution of highly crystalline CeO_2 nanoparticles measuring between 4-6 nm. The identification of Ni was difficult in HRTEM and STEM-HAADF modes due to lack of contrast between Ni and NiO phases. Nickel particles were instead located using EDX analysis, which suggested particle sizes between 5-8 nm. It was not possible to directly observe whether the nickel content existed as Ni, NiO, or Ni within the CeO_2 lattice.

HRTEM analysis of the d-5NiCe catalyst (Figure 1a) revealed a material nearly identical to **i-5NiCe**, with highly crystalline CeO_2 nanoparticles between 4-6 nm. Localization of Ni was

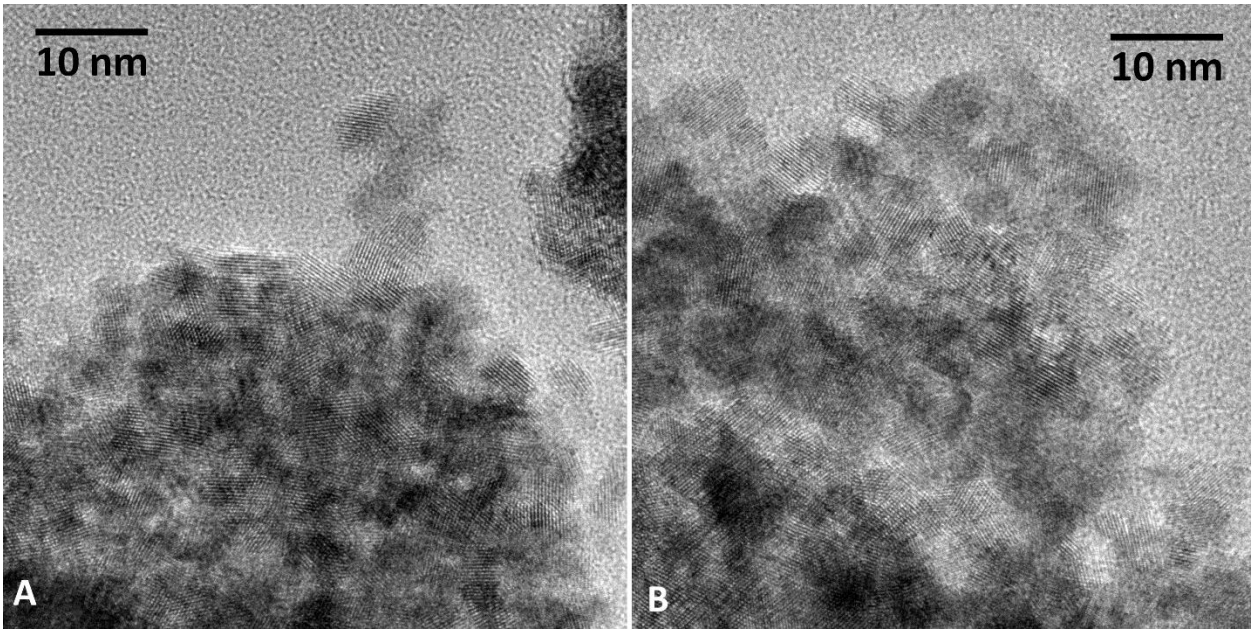

*Figure 1: HRTEM images of (a) **d-5NiCe** and (b) **i-5NiCe***

accomplished with EDX, as with the i-5NiCe sample. The nickel content was observed to be highly dispersed, due to the very low Ni EDX signal despite the nearly 5 wt% Ni loading.

4.2. Spectroscopic Characterization

Ex-situ synchrotron spectroscopic characterization of the doped mesoporous Ni/CeO_2

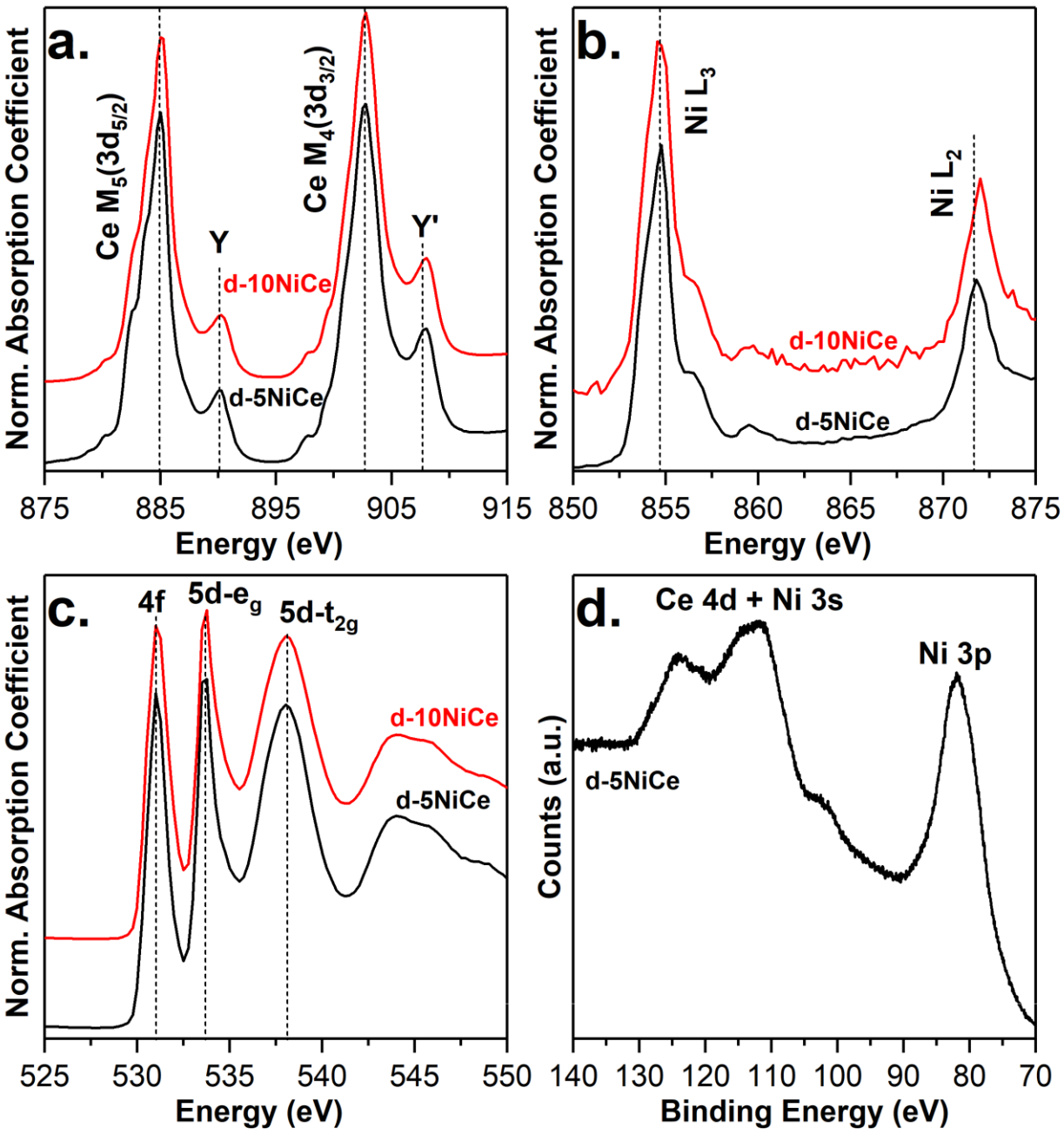

*Figure 2: (a) Ce $M_{4,5}$-edge, (b) Ni $L_{2,3}$-edge, and (c) O K-edge NEXAFS measured for **d-5NiCe** and **d-10NiCe** catalysts. (d) Ce 4d, Ni 3s, and Ni 3p XPS spectrum measured for **d-5NiCe**.*

materials was carried out using the NEXAFS and XPS techniques.

Cerium $M_{4,5}$-edge NEXAFS spectra were collected for the **d-5NiCe** and **d-10NiCe** samples (Figure 2a). The two main cerium features were observed at 885 eV (Ce M_5) and 902.5 eV (Ce M_4) for both samples. The separation between the features was 17.5 eV. Lower intensity features were also observed at 890.5 eV (Y) and 908 eV (Y'). These features are suggestive of CeO_2 in an unreduced state[18]. The majority of the cerium content in the as-prepared doped mesoporous Ni/CeO_2 catalysts likely exists as CeO_2, with little initial reduced ceria content.

Nickel L-edge NEXAFS was used in order to probe the state of nickel in the as-prepared **d-5NiCe** and **d-10NiCe** catalysts (Figure 2b)**.** Two sharp features were observed. The Ni L_3 feature was observed at 854.5 eV for both samples. The Ni L_2 feature was observed at 871.8 for the **d-5NiCe** catalyst and 872.0 eV for the **d-10NiCe** catalyst. This perceived difference may be due to the limits in the collected data quality. A smaller feature is visible overlapping with the main Ni L_3 peak around 856.5 eV. The presence of this feature, as well as the general shape of the spectrum and the high energy position of the Ni L_3 peak suggests that nickel is present predominantly in the Ni^{2+} oxidation state[19].

Oxygen K-edge NEXAFS spectra were also collected for the **d-5NiCe** and **d-10NiCe**, as reported in Figure 2c. Three features corresponding to the O1s to 4f, 5d-e_g, and 5d-t_{2g} transitions were clearly observed for both catalysts. These orbital transitions are characteristic of ceria[20, 21]. As with the Ce $M_{4,5}$-edge NEXAFS spectra, these measurements are suggestive of an unreduced CeO2 material, and may be readily differentiated from O K-edge NEXAFS spectra recorded previously for reduced ceria[22].

An XPS spectrum was collected for **d-5NiCe** in the region where the Ce 4d and Ni 3s features overlap, and where the Ni 3p feature may be observed (Figure 2d). Although the overlapping features here are ambiguous, the shape of the Ce 4d + Ni 3s region suggests an unreduced CeO_2 phase[23]. The Ni 3p feature is at a high energy position (82 eV), suggesting an oxidized state[24]. This data further corroborates the observations from the NEXAFS experiments, suggesting that the as-prepared doped catalysts consist of predominantly unreduced CeO_2 nanoparticles, and that the nickel content exists in the Ni^{2+} state.

4.3. Catalytic Activity

Water-gas shift catalytic activity was measured for all samples using an RGA quadrupole mass spectrometer during in-situ X-ray diffraction experiments. The CO_2 production recorded during the experiments is plotted for each catalyst in Figure 3a. Overall, the greatest CO_2 production was achieved with higher loadings of nickel prepared using the in-situ doping method. Notably, **d-5NiCe** and **d-10NiCe** exhibited activity at the lowest temperature, 250°C. An attempt was made, however, to normalize WGS by nickel content. This was done by dividing the peak CO_2 production at each temperature step by the approximated (maximum) nickel

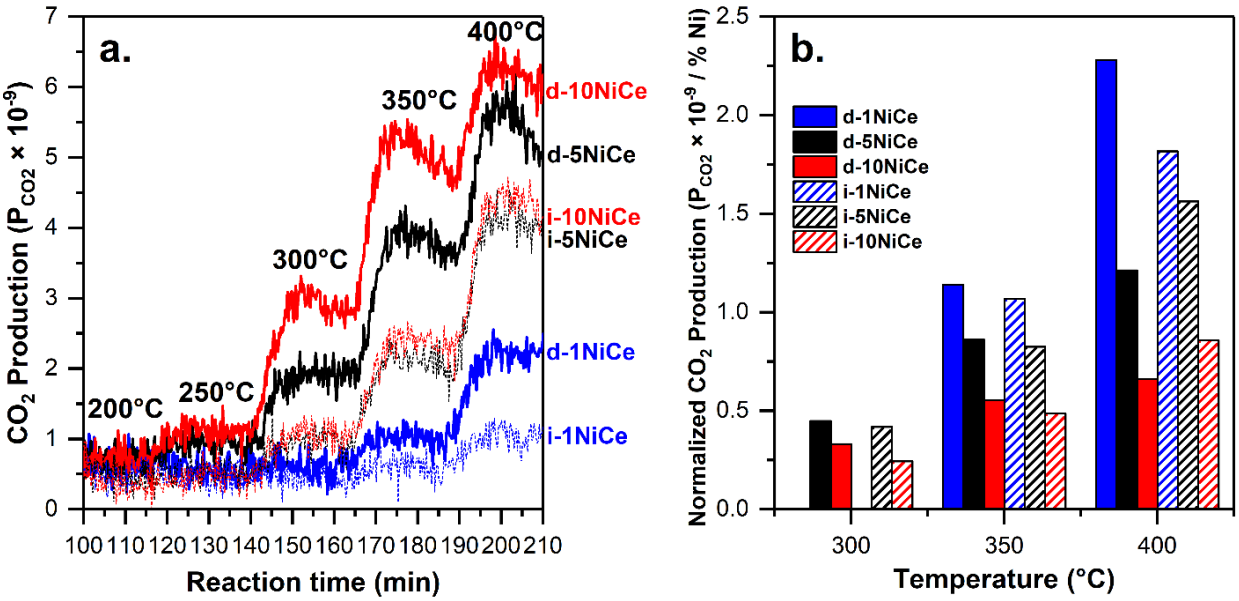

Figure 3: Catalytic activity of mesoporous various Ni/CeO_2 catalysts. (a) CO_2 production as measured by RGA. (b) CO_2 production normalized to approximate nickel content.

content (wt%) of each sample, assuming that nickel serves as the active site that binds CO. The results of this analysis are presented in Figure 3b. From here it may be inferred that lower loadings of nickel, particularly the **d-1NiCe** sample, may yield more activity per unit nickel, and therefore present a greater concentration of active sites in the catalyst.

An Arrhenius study was carried out in order to compare the WGS activity of the **d-5NiCe** catalyst with similarly prepared in-situ doped 5 wt% copper and cobalt loaded catalysts. The results of this study were normalized to sample weight and are reported alongside bare mesoporous CeO_2 activity in Figure S6. We have previously reported mesoporous Cu/CeO_2 as an active catalyst for the low to intermediate temperature WGS reaction[2], and mesoporous Co/CeO_2 as a superior catalyst for the high temperature WGS[25]. The nickel loading underperforms copper in the low temperature regime, and underperforms Co in the high temperature regime, but displays comparable WGS activity to both in the 350 to 400°C range. Previously reported activity trends for metals supported on Al_2O_3 indicate that both copper and cobalt should outperform nickel in the low temperature WGS[26]. For these mesoporous CeO_2 materials, however, nickel performs significantly better than cobalt. This difference may be due to the facile and rapid activation of H_2O that was previously reported for Ni/CeO_x systems[27].

4.4. Ex-situ X-ray Diffraction

X-ray diffraction patterns collected for fresh mesoporous Ni/CeO_2 catalysts are presented in Figure 4. For all samples, the fluorite CeO_2 phase was predominant, with broad features suggesting small nanoparticles. A very small minority species was observed around $2\theta = 11.6$. This feature does not correspond to any possible nickel or cerium species and is likely a contaminant.

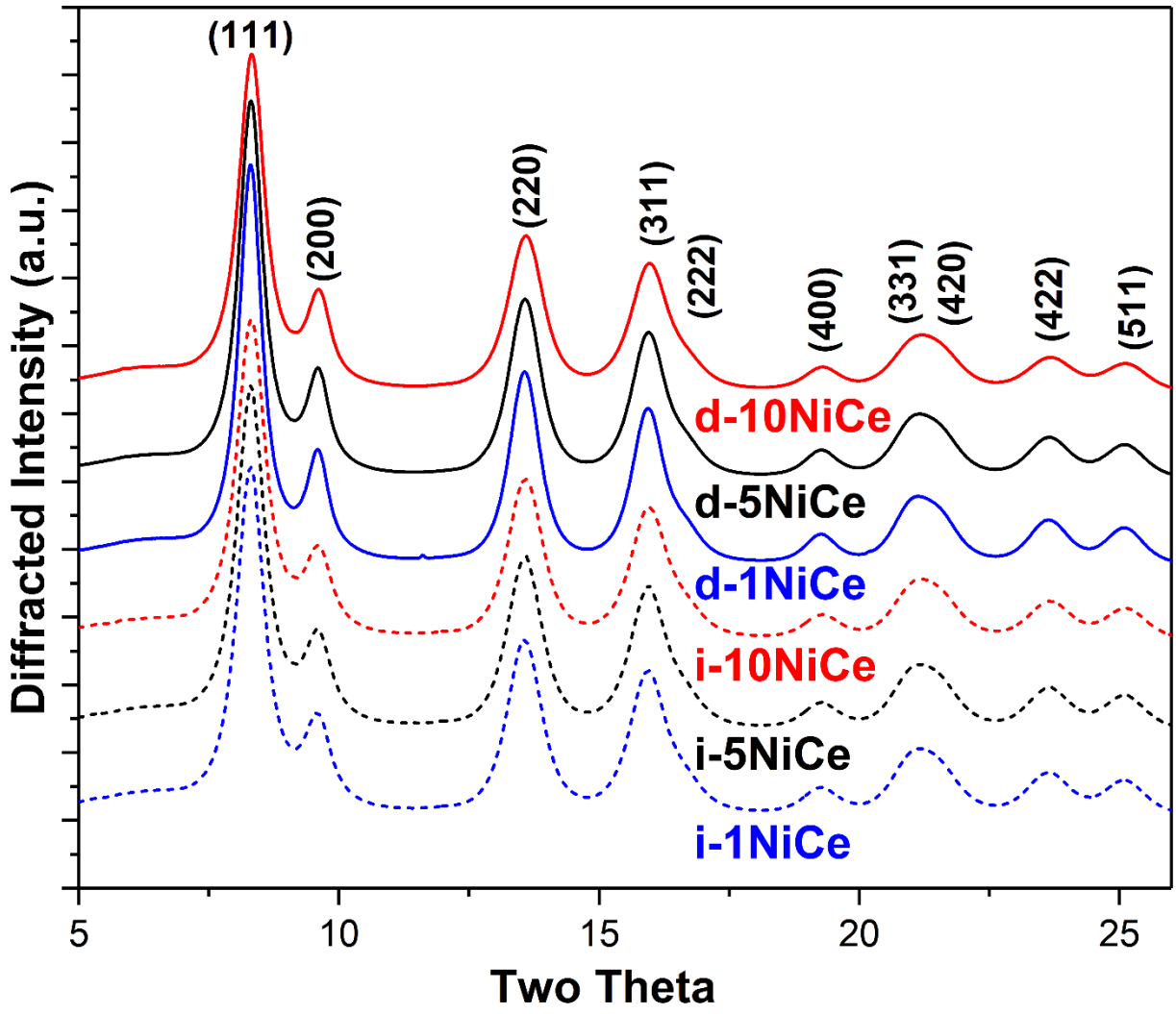

Figure 4: Ex-situ X-ray diffraction patterns collected for mesoporous Ni/CeO_2 catalyst.

No nickel or nickel oxide phase was observed in any catalyst. In the HRTEM studies, nickel was observed to exist within regions measuring 5-8 nm. Crystalline Ni or NiO particles of this size would be readily visible in XRD. Since no amorphous regions were detected using HRTEM, it is therefore likely that the nickel content exists within the CeO_2 lattice, with the Ni^{2+} ion (r = 0.69 Å) replacing the Ce^{4+} cation (r = 1.14 Å). This replacement would generally result in the shrinking of the lattice size and creation of oxygen vacancies in the CeO_2 fluorite lattice to achieve charge balance.

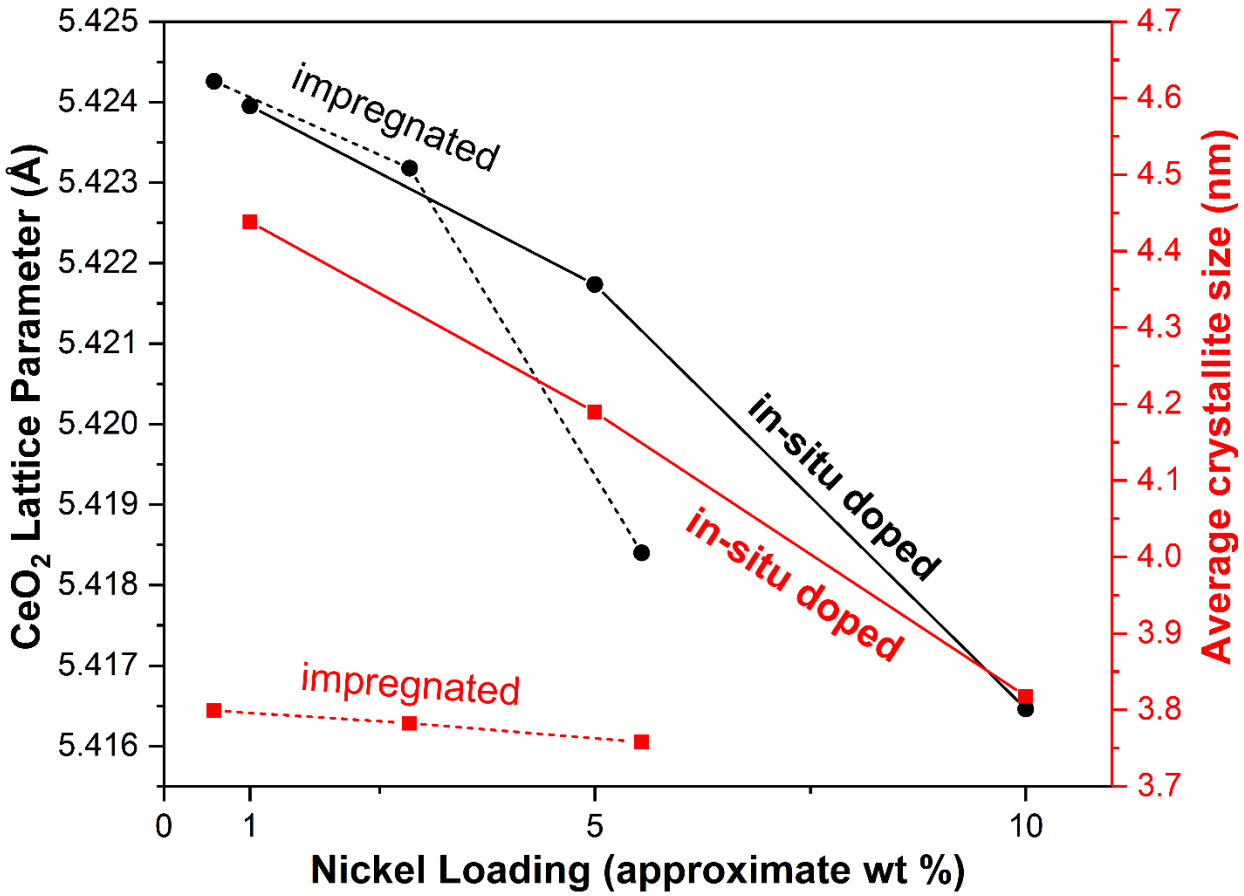

Figure 5: CeO_2 lattice parameter and average crystallite sizes obtained for mesoporous Ni/CeO_2 catalysts under ex-situ conditions via Rietveld refinement of models to fit XRD data.

Rietveld refinement[16] of models fit to the ex-situ XRD data was used to generate lattice parameters and average crystallite sizes for all the mesoporous Ni/CeO_2 catalysts. The results were plotted against the approximated Ni weight percentage of each catalyst (Figure 5).

As expected, the CeO_2 lattice was observed to decrease with increasing nickel content, further suggesting that nickel exists as Ni^{2+} ions replacing Ce^{4+} ions in the CeO_2 fluorite lattice. Interestingly, the lattice parameter of the **i-10NiCe** sample is substantially lower than that of the **d-5NiCe** sample, despite having a lower potential loading. It is possible that lattice parameter is not a function of nickel loading alone, however the Ni concentrations for all samples are simple estimates that assume inclusion of 100% of the nickel content introduced during preparation, which was likely not the case for any catalyst.

The CeO_2 particle size calculated for the impregnated samples was substantially lower than for the in-situ doped samples. Lower particle sizes are usually an indicator of higher surface area, better dispersion, and promotion of catalytic activity. Despite the lower crystallite sizes of the impregnated samples, however, the in-situ doped samples were observed to out-perform in WGS catalytic activity, suggesting that activity may not simply be a function of surface area, and that metal-support interactions at the surface of the catalyst must also be considered. The variability in average particle size was small, however, with all samples falling between 3.75nm and 4.4nm.

4.5. In-situ X-ray Diffraction

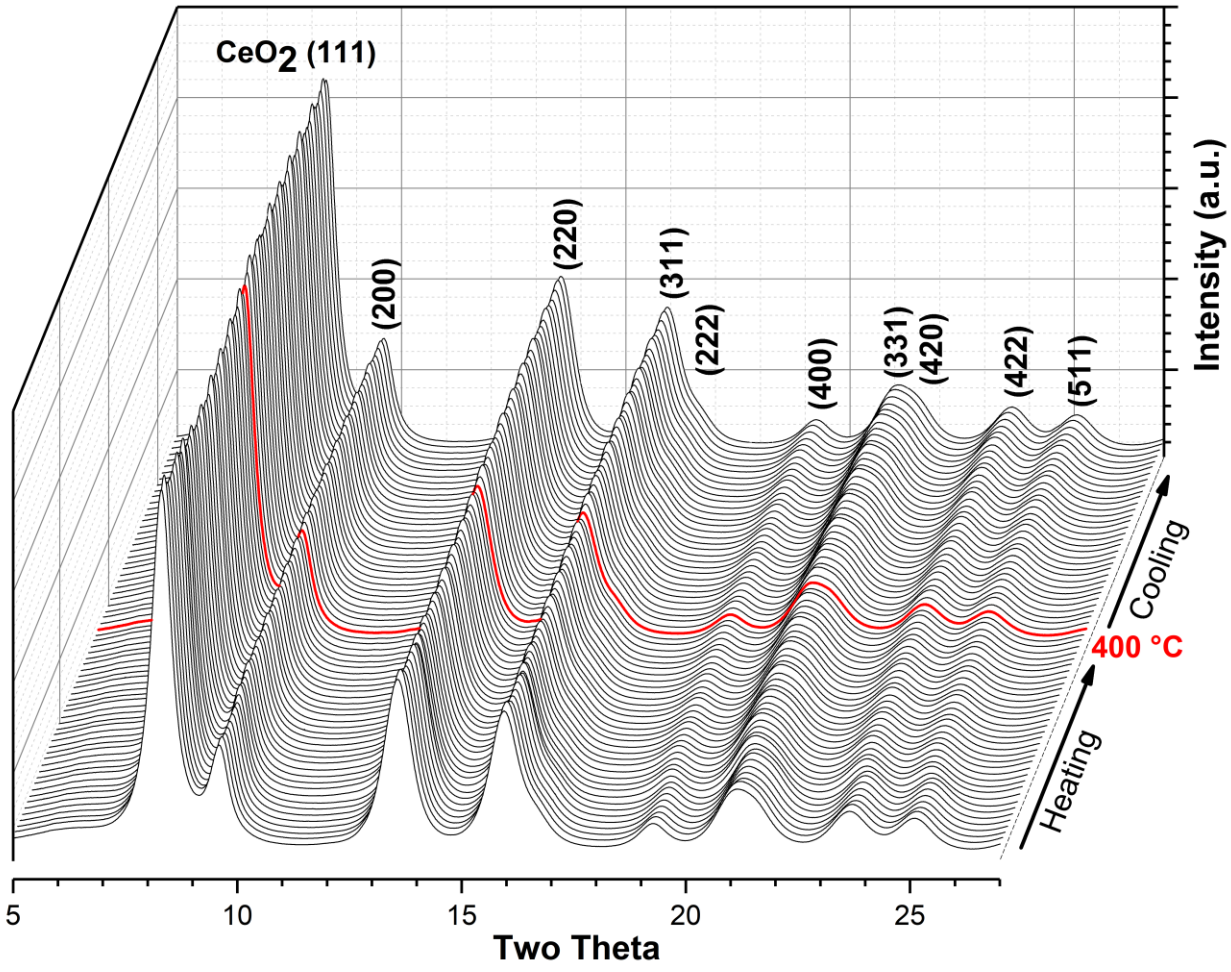

*Figure 6: In-situ X-ray Diffraction plot for **d-5NiCe**.*

In-situ XRD was employed in order to study the structure of the mesoporous Ni/CeO_2 materials under WGS reaction conditions. Diffraction patterns were collected continuously as each sample was heated stepwise to 400°C under WGS conditions (5% CO, 3% H_2O in He @ 10 cc/min) and then cooled stepwise to room temperature. Figure 6 depicts every 10th diffraction pattern measured for **d-5NiCe** during this experiment. This plot looks nearly identical to those generated for all other mesoporous Ni/CeO_2 samples. No nickel phase was observed at any point for any catalyst. In order to further analyze the structure of these materials under reaction conditions, Rietveld refinement was used to obtain the CeO_2 lattice parameter from each diffraction pattern. The resulting lattice parameters were plotted over time alongside CO_2 production. The lattice parameters were also plotted against temperature in order to better visualize temperature-related structural transitions. These two-part plots were compiled for each of the samples: **d-5NiCe** (Figure 7), **i-5NiCe** (Figure 8), **d-1NiCe** (Figure S1), **d-10NiCe** (Figure S2), **i-1NiCe** (Figure S3), and **i-10NiCe** (Figure S4).

The lattice parameter of each sample was observed to change under WGS conditions in response to temperature. An initial decrease in lattice parameter was observed for all samples as they were heated to 100°C. This decrease is likely due to desorbing precursor and contaminant species, since no pretreatments were carried out prior to the in-situ WGS experiments.

Between 100 and 200°C, depending on the catalyst, a sharp increase in lattice parameter was observed. These increases may be visualized in the temperature plots as isothermal or nearly isothermal increases in CeO_2 lattice parameter upon heating (red lines). The cause for these isothermal expansions was likely the reduction of cerium in the CeO_2 fluorite lattice. Since the Ce^{3+} ion (r = 0.97 Å) is larger than the Ce^{4+} ion (r = 1.14 Å), reduction of ceria results in expansion of the lattice. This expansion process is further amplified by the generation of oxygen

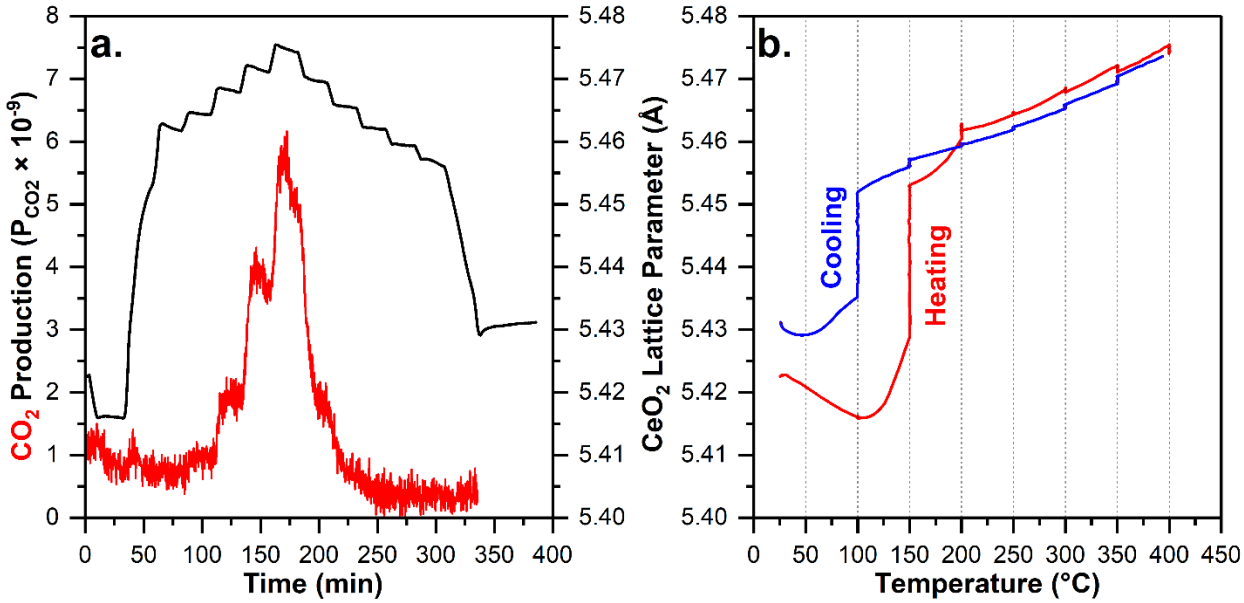

*Figure 8:(a) CeO_2 lattice parameter from **d-5NiCe** with CO_2 production. (b) CeO_2 lattice parameter over temperature*

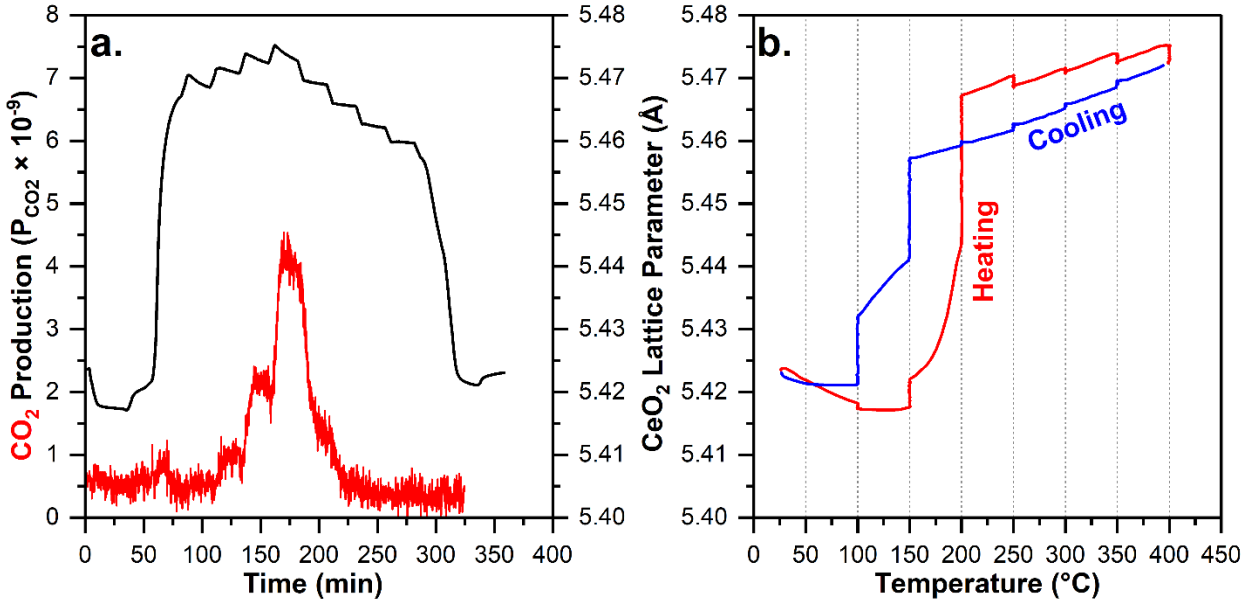

*Figure 7: (a) CeO_2 lattice parameter from **i-5NiCe** with CO_2 production. (b) CeO_2 lattice parameter over temperature*

vacancies in the partially reduced oxides to restore charge balance[28, 29]. This effect was observed to reverse upon cooling, between 200 and 100°C depending on the catalyst. This is due to the re-oxidation of ceria, likely from the H_2O content in the WGS reactant gas stream.

At higher temperatures, the CeO_2 lattice parameter was observed to change in approximate linear relationship with temperature. This change may be clearly visualized in the temperature plots due to its linear nature. This component represents the thermal expansion upon heating, and subsequent thermal contraction of the lattice upon cooling.

Some catalysts, such as **d-5NiCe**, achieve a stable lattice at higher temperatures resulting in almost exclusively thermal lattice changes within the active temperature range of the catalyst. On the other hand, an unstable lattice was observed at high temperatures for **i-1NiCe**, with both thermal and redox expansion components being exhibited up to 400°C. A relationship between the stability of the lattice in the active temperature range and activity was not readily apparent, particularly when considering activity normalized to nickel content. The reduction of nickel in the CeO_2 fluorite lattice from Ni^{2+} (r = 0.69 Å) to Ni^0 (r = 2.00 Å) is a confounding factor in the stability of the lattice at higher temperatures, as it would have an additional expansive effect.

The temperature window of the stable lattice state, where thermal changes prevail, was observed to have a strong dependence on the preparation method of the catalysts. Isothermal expansion of the lattice upon heating (Ce^{4+} to Ce^{3+} reduction) was observed between 100 and 150°C for the in-situ doped samples, compared to between 150 and 200°C for the impregnated samples. Similarly, the re-oxidation of the lattice occurs at a higher temperature for impregnated samples (200 to 100°C) than for the in-situ doped samples (150 to 100°C). The result is that the stable lattice state persists over a larger temperature range for in-situ doped samples. This effect is best observed in Figure 9, where all lattice trends were plotted together over time. The earlier attainment of the stable lattice state in **d-5NiCe** and **d-10NiCe** (150°C for both) may be

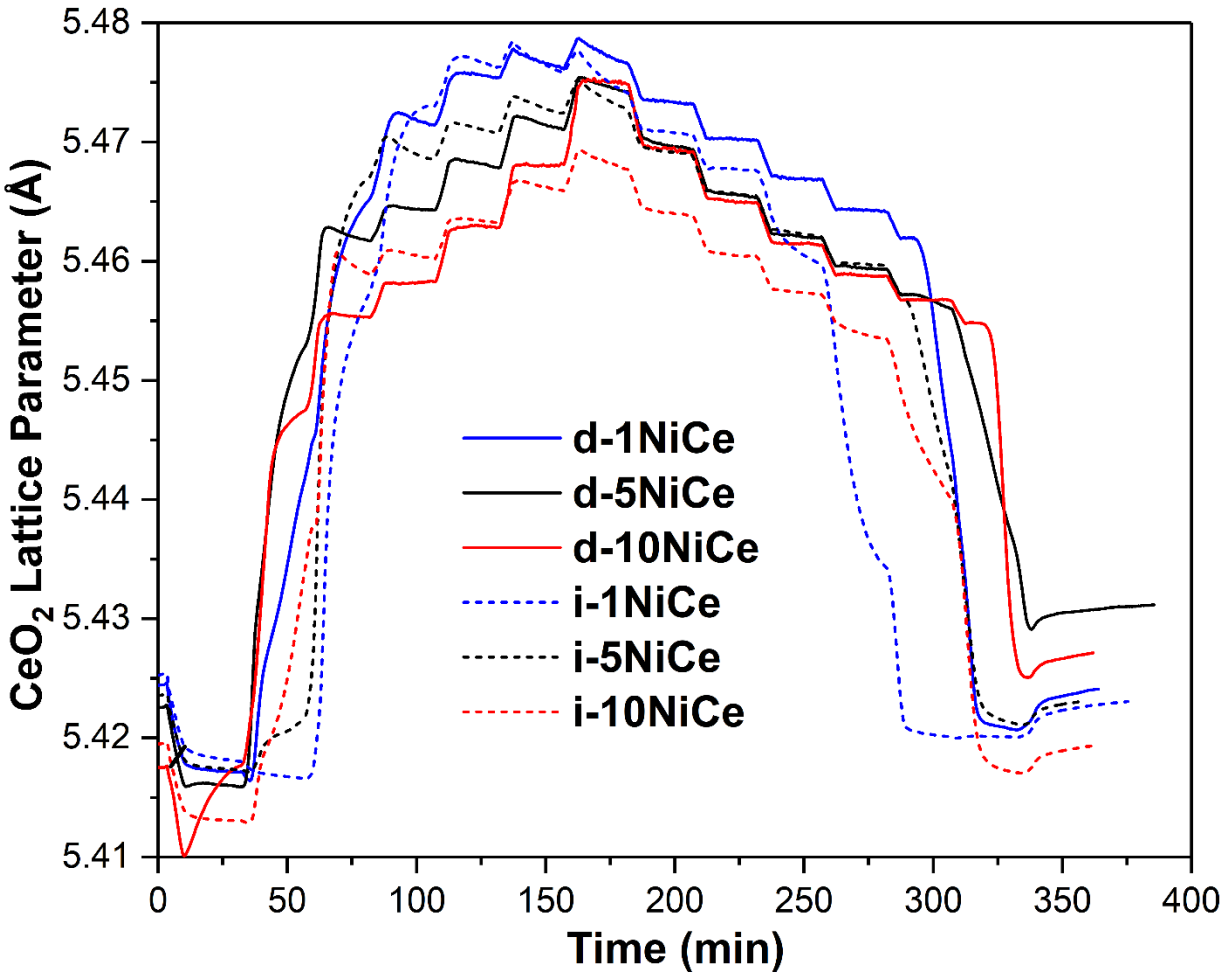

Figure 9: CeO_2 lattice parameters over time for mesoporous Ni/CeO_2 catalysts under WGS conditions.

correlated with the lower temperature at which first activity was observed (250°C for these samples vs. 300 to 350°C for the rest). On the other hand, **i-1NiCe** was only observed to exhibit WGS activity at 350 and 400°C, while also exhibiting the smallest stable lattice window (above 200°C).

The total degree of lattice expansion was observed to generally trend with nickel concentration. Interestingly, these trends are separate for the impregnated and in-situ doped samples despite differences in actual nickel content. This effect is visualized easily in Figure 9. Generally, a greater degree of lattice expansion would imply a greater degree of cerium

reduction and a greater concentration of oxygen vacancies, which may serve as active sites for H_2O dissociation. The greatest degree of expansion was observed for the **d-1NiCe** and **i-1NiCe** catalysts, which show the greatest activity (at 350 to 400°C) when normalized to nickel content. These catalysts do not show the greatest *total* catalytic activity, however, suggesting that there may be a metal-support relationship between the greater concentration of active nickel sites and greater availability of oxygen vacancy sites. It is not known whether this relationship is causal or coincidental.

4.6. In-situ X-ray Absorption Near-edge Structure (XANES)

In-situ Ni K-edge XANES was carried out for the **i-5NiCe** sample in order to determine the chemical state of nickel under WGS reaction conditions. Standard measurements were also recorded for NiO and Ni metal samples. The results are plotted in Figure 10.

The XANES spectra measured for **i-5NiCe** feature a peak at 8350 eV, in line with the NiO standard. The shape of the spectrum, as well as the positions of the edge and white line at room temperature suggest a sample that is almost entirely Ni^{2+}. As the sample was heated, the intensity of the peak at 8350 eV was observed to decrease. Meanwhile, the intensity of the pre-edge feature was observed to increase. Similarly, the portion of the spectra around 8370 eV was also observed to increase in intensity.

Isosbestic points were identified around 8340 eV, 8357 eV, and likely 8388 eV, suggesting that the process involves the transition between two species. These isosbestic points line up roughly with intersection points observed between Ni and NiO standards. Upon heating **i-5NiCe** under WGS reaction conditions, partial reduction of Ni^{2+} to Ni^0 occurs. Linear

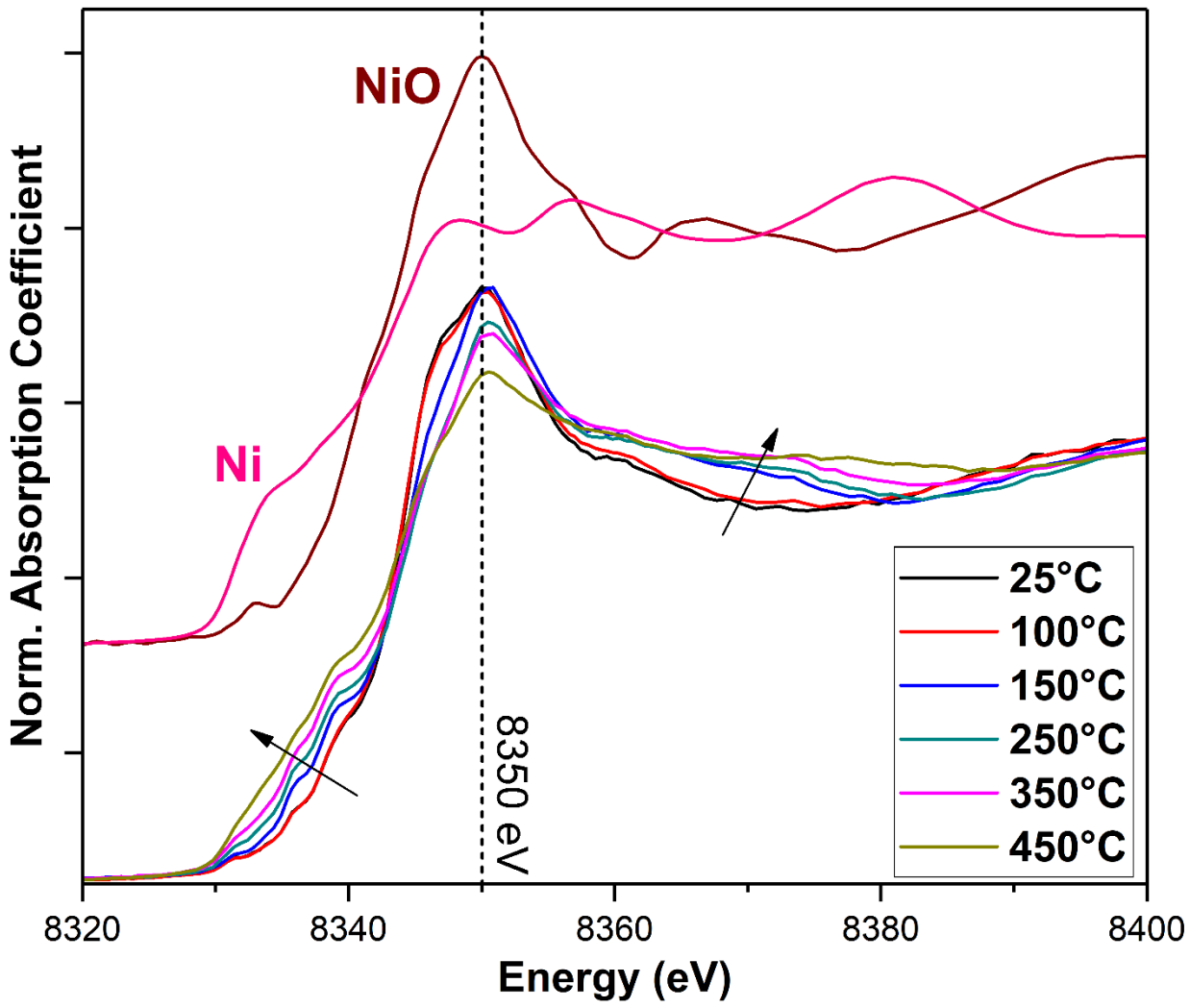

*Figure 10: In-situ Ni K-edge XANES collected for **i-5NiCe** under WGS reaction conditions.*

combination analysis (LCA) was used in order to more closely examine the degree of this reduction with temperature. The results of this analysis are plotted in Figure 11.

Linear combination analysis of Ni and NiO standards indicates that the nickel content in the as-prepared **i-5NiCe** catalyst at room temperature consists of almost entirely Ni^{2+}. No reduction occurs at 100°C, however reduction begins to occur upon heating to 150°C and beyond. This catalyst was found to first exhibit WGS catalytic activity at 300°C, at which point the nickel content was 35-40% metallic. Nickel was observed to continue to reduce up to 450°C.

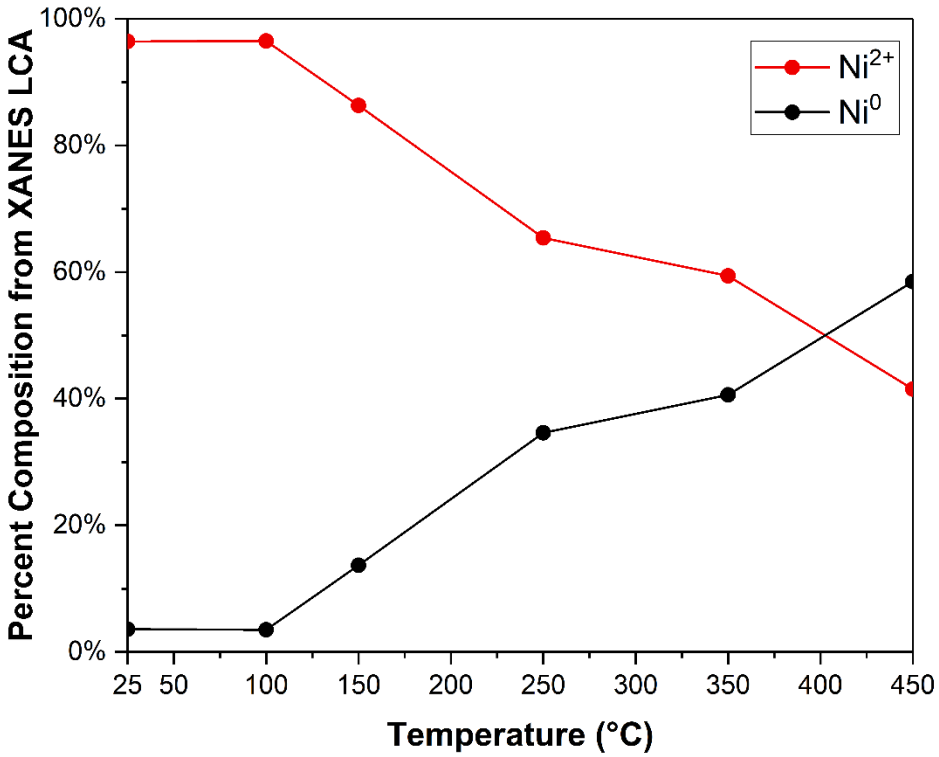

*Figure 11: Results of linear combination analysis of Ni K-edge XANES data collected for **i-5NiCe**.*

The highest activity measured for all catalysts was at 400°C. For **i-5NiCe**, nickel was approximately 50% metallic at this point. Activity was not measured beyond 400°C.

Although XANES experiments were not carried out for other mesoporous Ni/CeO_2 catalysts, it is very likely that Ni^{2+} to Ni^0 reduction plays a crucial factor in WGS catalytic activity for all samples. While specific reduction rates would likely vary, in-situ XRD data strongly suggests that nickel remains within the CeO_2 fluorite lattice throughout the course of the reaction in all samples. Therefore, a redox relationship exists between the nickel, cerium, and oxygen species in the lattice. Reduction of nickel could cause additional generation of catalytically important oxygen vacancies, which would benefit those catalysts with greatest degree of nickel reduction at the temperatures within the active range.

4.7. In-situ DRIFTS: Active Surface Chemistry

The surface chemistry of the mesoporous Ni/CeO_2 catalysts under WGS conditions was studied using in-situ DRIFTS experiments carried out for **d-5NiCe** and **i-5NiCe**.

Representative DRIFTS spectra taken at each temperature step for **d-5NiCe** are presented in Figure 12. Gas phase H_2O, a broad feature around 3200 cm^{-1}, was present at room temperature along with molecularly adsorbed H_2O (1650 cm^{-1}). These features were removed upon heating. The development of hydroxyl species was observed around 3650 cm^{-1}. Two formate regions were observed in the 3000-2600 cm^{-1} and 1700-1200 cm^{-1} regions. A carbonate feature was observed around 855 cm^{-1}.

Gas phase CO_2 production (2350 cm^{-1}) was recorded as early as 150°C. In contrast to the

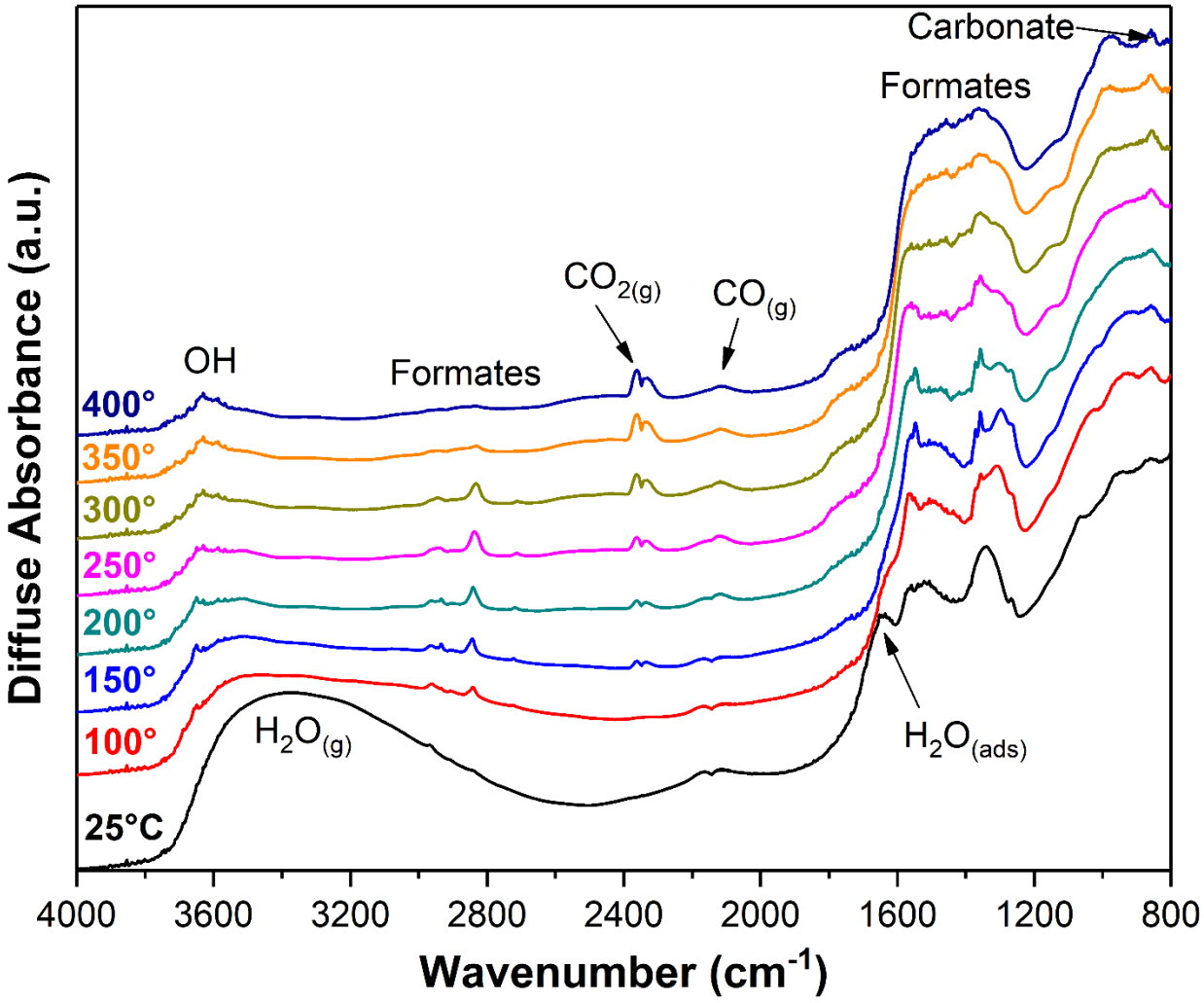

*Figure 12: In-situ DRIFTS: **d-5NiCe** under WGS conditions.*

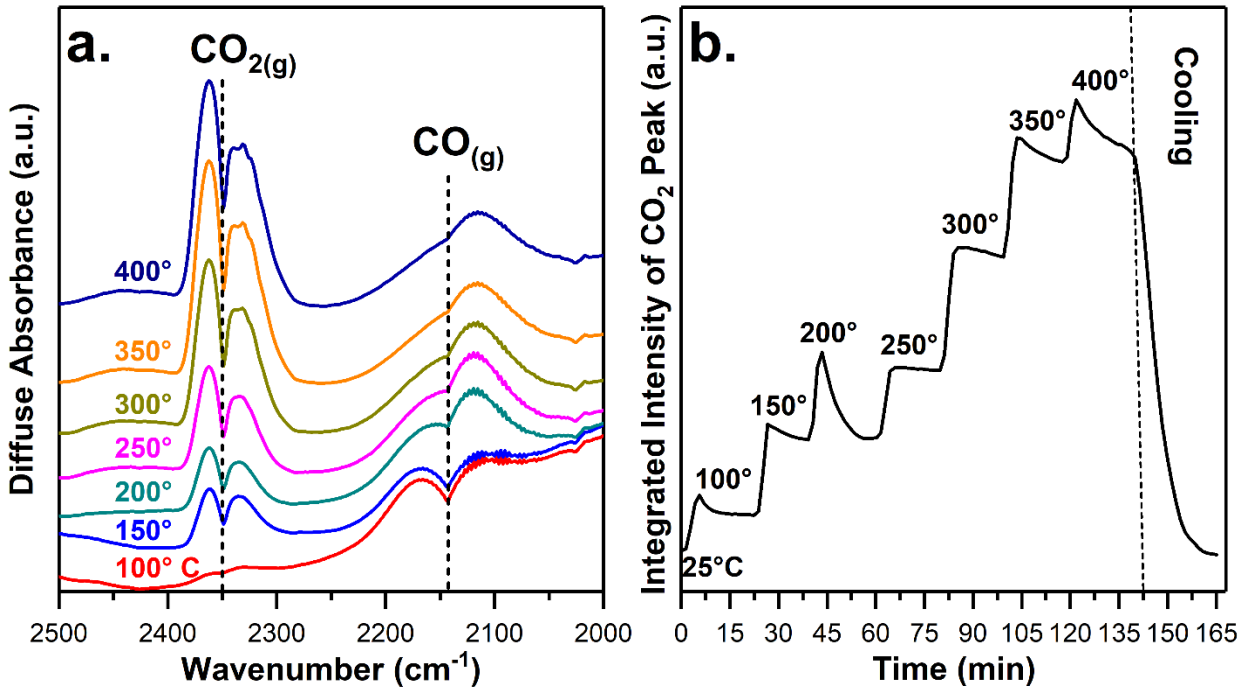

*Figure 13: (a) Representative DRIFTS spectra of CO and CO_2 region for **d-5NiCe** under WGS conditions and (b) integrated intensity of CO_2 feature over time.*

activity measurements in Figure 3, this is a much lower temperature. In order to more closely examine this CO_2 production and explore the differences with prior activity measurements, the CO_2 doublet feature was integrated over time. The resulting activity curve was plotted next to a detailed image of the CO/CO_2 region in Figure 13. Although this activity curve is not directly comparable to the activity measurements from Figure 3, these data were compared to RGA measurements taken during the DRIFTS experiment. In Figure S5, the plot from Figure 13b was superimposed over the RGA CO_2 signal and scaled to fit. The result was an almost perfect match, establishing the integration of the gas phase CO_2 DRIFTS feature as a valid method of obtaining a qualitative WGS activity curve in these experiments.

There are at least three reasons for the significant differences between the activity measurements reported in Figure 3 and the activity measurements reported in Figure S5. First, the catalyst was pre-treated in helium at 200°C for 2 hours prior to the DRIFTS experiments.

This pre-treatment was not carried out during the in-situ XRD experiments due to beamtime constraints, and may impact the profile of the reaction, particularly at lower temperatures. Second, the RGA instrument setup for the in-situ XRD experiments was different from the RGA instrumentation used for the DRIFTS experiments. The in-situ XRD RGA data contained a significant amount of noise which could have covered up low temperature activity. Third, the reactor architecture of the Clausen flow reactor is significantly different from the DRIFTS reaction cell, which is not intended to approximate a plug flow system and is limited by a large area of dead volume in the dome. Because of these reasons, DRIFTS reactivity data should be treated as separate from the activity data reported in Figure 3.

A hydroxyl feature at 3650 cm^{-1} was observed between 100 and 200°C. At higher temperatures, this is replaced by a broad hydroxyl feature around 3630 cm^{-1}. The presence of hydroxyls on the catalyst surface is direct evidence of the dissociation of H_2O, a critical step in the WGS reaction. Since the position of the formate changes at higher temperatures, it is likely that the reaction pathway is modified.

In the formate regions of the DRIFTS spectra collected for the **d-5NiCe** catalyst, both monodentate[30] and bidentate[31] formate species were identified, as in Table 2.2. Analysis of these regions was carried out by integrating individual features and plotting the integrated intensity over time (Figure 14). Two prominent monodentate formate features at 2968 and 1263 cm^{-1} were identified, and these were observed to decrease in intensity upon heating under WGS conditions (Figure 14c). This species likely serves as a spectator or catalytic poisoning agent, as there is no tracking activity and it does not appear prominent at the active temperature range.

Bidentate formate features were also observed at 2933, 2840, 2720, 1355, 1371, and 1550 cm^{-1}. The features at 2840 and 2720 cm^{-1} were observed to shift and overlap with another feature at higher temperatures and did not track in intensity with the other bidentate formate peaks observed, suggesting the presence of an additional carbonaceous species (likely a formate

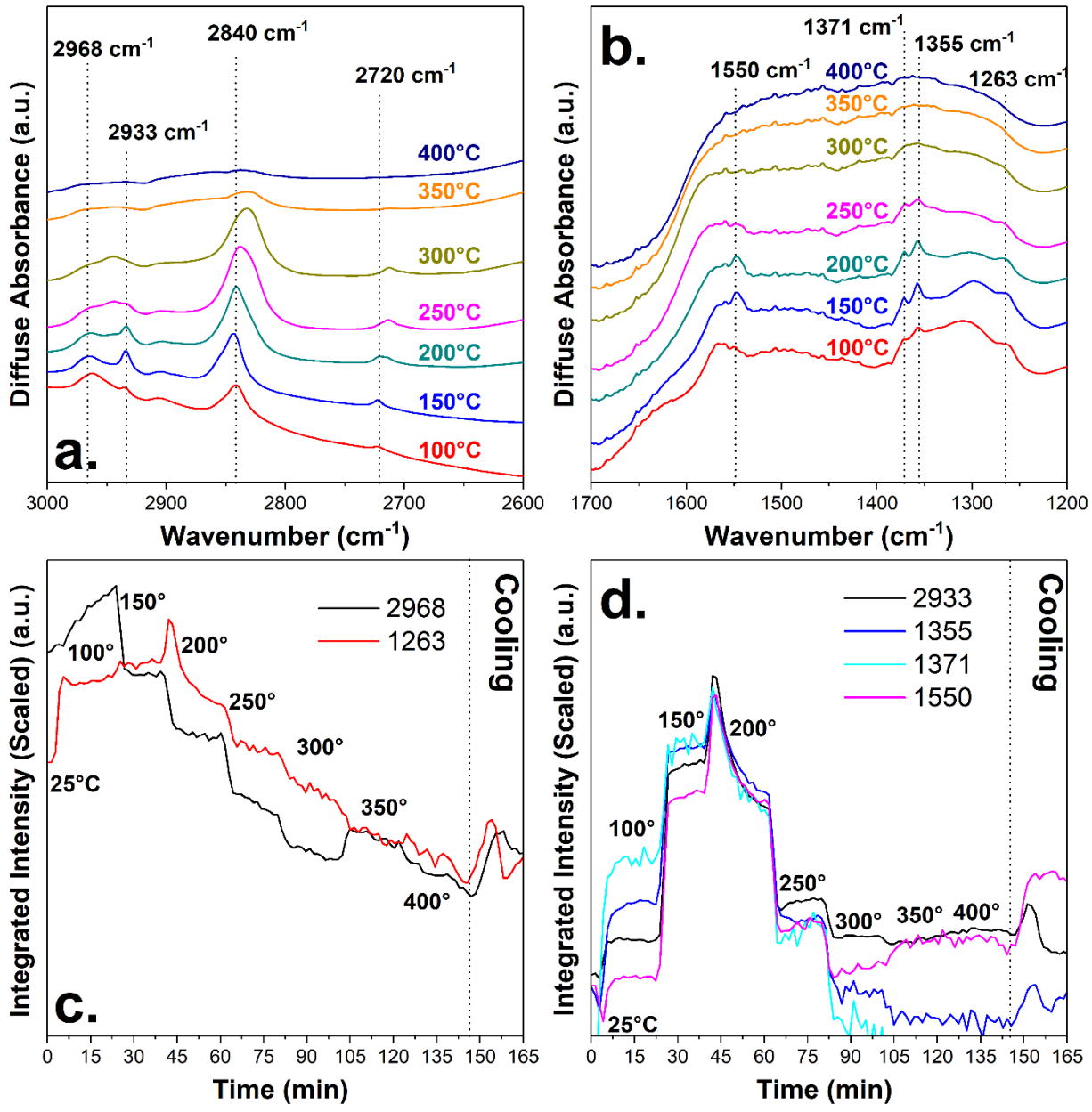

*Figure 14: (a,b) Representative DRIFTS spectra of the formate regions for **d-5NiCe** under WGS conditions, (c) integrated intensities of monodentate formate features, and (d) integrated intensities of bidentate formate features.*

reconfiguration) at the 250 to 350°C temperature range. The clearly defined bidentate formate features were integrated and plotted in Figure 14. Interestingly, the integrated peaks all feature a sharp rise followed by a decrease at the 200°C step. This behavior is closely correlated with a sharp, rapidly deactivating peak in CO_2 production at the same 200°C step, as seen clearly in Figures 13b and S5. This close correlation with activity suggests that bidentate formate may be playing an active role in the WGS reaction, potentially as an intermediate species in an associative mechanistic pathway. At the temperatures when the catalyst is most active, these features were no longer observed. A different mechanistic profile (likely redox) may prevail at the higher temperatures, particularly as the nickel content is significantly reduced to a metallic state. This possibility is also supported by the changes observed in the hydroxyl species.

A carbonate feature around 855 cm^{-1} was observed to increase in intensity with temperature. This species was previously identified as a potential intermediate in the WGS reaction over bare mesoporous ceria. Because this feature is prominent when activity is highest, it is possible that it may serve as a part of an associative type reaction pathway. This pathway would be different from the potential bidentate formate pathway, however, and would compete with a likely redox mechanism. Another possible role for the surface carbonate species would be that of a spectator, as it does not seem to inhibit activity.

In-situ DRIFTS analysis for **i-5NiCe** under WGS reaction conditions was also carried out. Representative DRIFTS spectra at each temperature step are presented in Figure 15. The features and trends observed for **i-5NiCe** were largely the same as those observed for **d-5NiCe**.

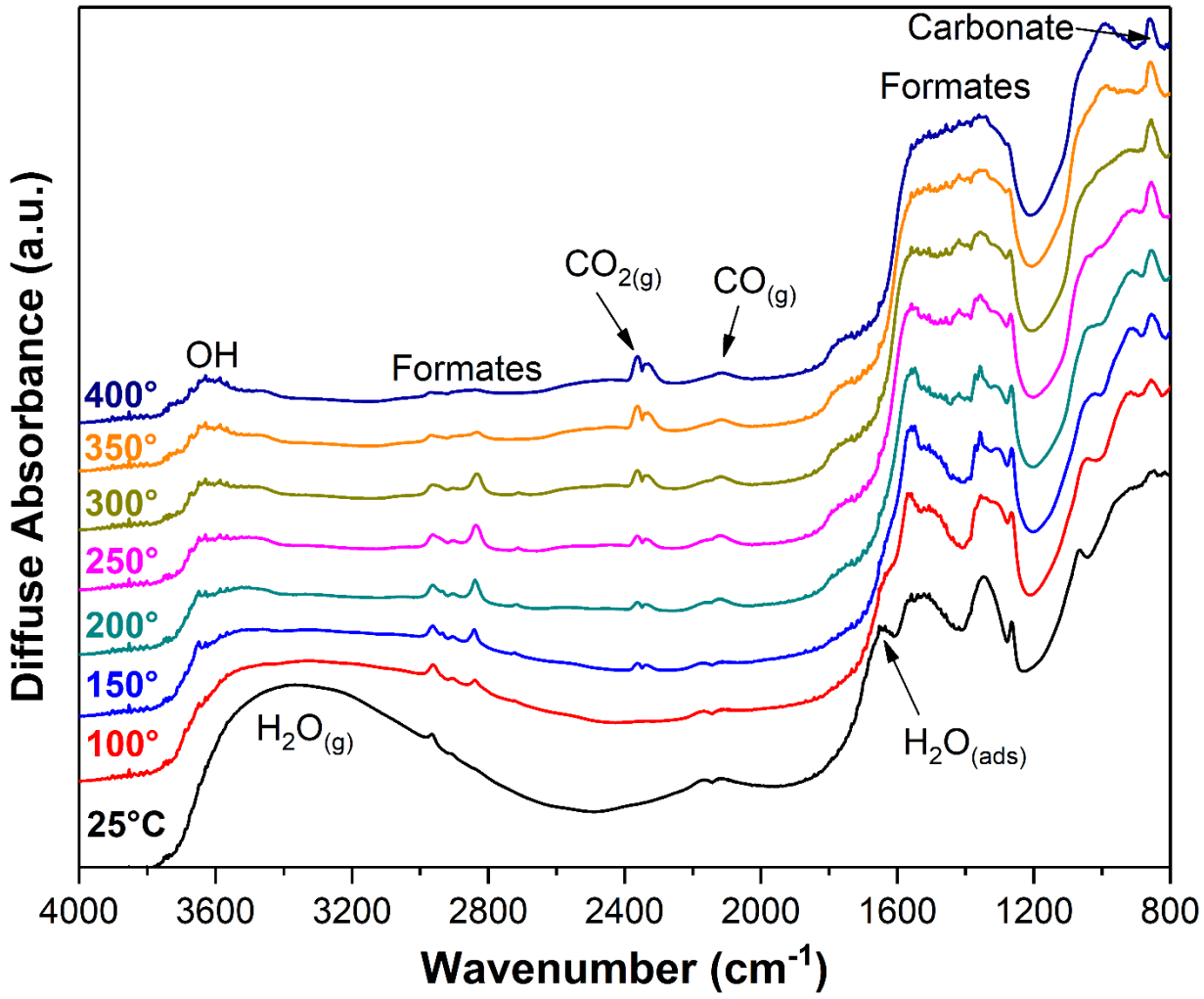

*Figure 15: In-situ DRIFTS: **i-5NiCe** under WGS conditions.*

The measured activity via CO_2 gas phase feature integration was comparable in shape and magnitude to that measured for **d-5NiCe**. The CO/CO_2 DRIFTS region and integrated intensity of the CO_2 feature over time are plotted for **i-5NiCe** in Figure 16. Activity plots from both **d-5NiCe** (Figure 13b) and **i-5NiCe** (Figure 16b) were also plotted together on a shared scale in Figure 17. The activity of the two catalysts in the 100 to 250°C temperature range was nearly identical. The in-situ doped catalyst, however, displayed higher activity at temperatures above 250°C, however, similarly to the results recorded in Figure 3.

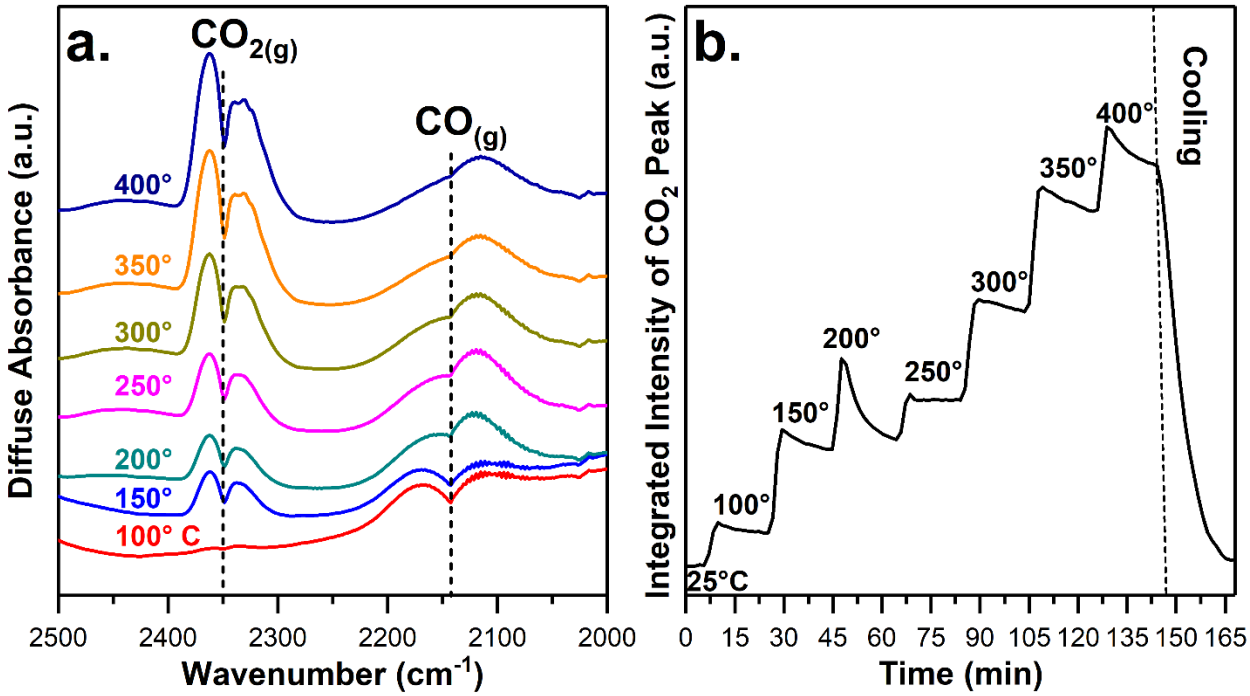

*Figure 16: (a) Representative DRIFTS spectra of CO and CO_2 region for **i-5NiCe** under WGS conditions and (b) integrated intensity of CO_2 feature over time.*

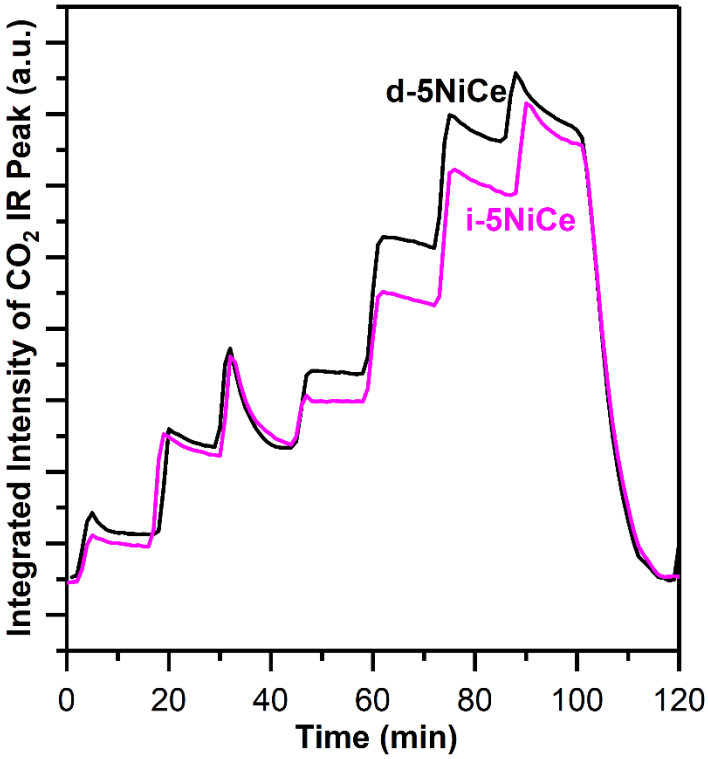

*Figure 17: CO_2 production by **d-5NiCe** (black) and **i-5NiCe** (purple) from DRIFTS.*

The hydroxyl and bidentate formate features recorded for **i-5NiCe** followed the same trends as those recorded for **d-5NiCe**, including the sharp peak in bidentate formate intensity at 200°C, which correlates with activity. The shift and overlap were also observed in the 2840 and 2720 cm^{-1} features after 250°C, and bidentate formate was nearly undetectable above 300°C. These observations suggest an associative pathway involving bidentate formate at lower temperatures. This pathway would yield nearly identical activity to **d-5NiCe** at lower temperatures. At higher temperatures, a redox mechanism would favor the greater nickel content of **d-5NiCe**, yielding higher activity.

The monodentate formate features measured for **i-5NiCe** at 2965 and 1263 cm^{-1} had much greater intensity at all temperatures than those measured for **d-5NiCe** and were evident at temperatures as high as 350°C. Additionally, the carbonate feature was much more intense at all temperatures on **i-5NiCe**. It is possible that associative pathways involving these carbonaceous species (particularly carbonate) are more prominent at high temperatures on the **i-5NiCe** catalyst due to its lower nickel content, however it is also possible that these species simply serve as spectators and do not have a great impact on WGS catalytic activity.

Overall, the **d-5NiCe** and **i-5NiCe** catalysts displayed very similar surface chemistry during the WGS reaction, despite the difference in nickel content and preparation method. From HRTEM and XRD analysis, nickel exists within the CeO_2 lattice regardless of preparation method, which suggests that the catalysts would have similar types of active sites (although active site concentrations may differ). Notably, **i-5NiCe** exhibits greater catalytic activity per unit nickel (Figure 3b). Since the predominant reaction mechanism at higher temperatures is likely a redox pathway involving metallic nickel, the nickel sites present with lower Ni concentrations in the lattice are more active for the WGS reaction.

5. Conclusions

Mesoporous Ni/CeO_2 catalysts with variable nickel content were prepared using two different synthesis methods. Microscopy of the materials revealed highly crystalline CeO_2 nanoparticles in the 4-6 nm range. Nickel content was observed to be highly dispersed within CeO_2 nanoparticles, likely within the CeO_2 fluorite lattice. X-ray diffraction analysis revealed CeO_2 as the single crystalline phase under WGS reaction conditions, further confirming the location of nickel within CeO_2, regardless of Ni concentration or preparation method. Spectroscopic methods were used to determine the as-prepared state of the materials to be largely composed of unreduced CeO_2 and nickel in the Ni^{2+} state.

The mesoporous Ni/CeO_2 materials were found to be active for the water-gas shift reaction. Activity generally favored in-situ doped catalysts and higher nickel loadings. When normalized to nickel content, however, the most active catalyst was the in-situ doped 1% Ni/CeO_2 (**d-1NiCe**) material, and activity generally favored lower Ni loadings, suggesting that these materials have more potent nickel active sites.

In-situ XRD and XANES under WGS conditions were used to identify the active phase of all catalysts as a stable, partially reduced CeO_2 fluorite lattice with Ni^{2+} ions and Ni^0 atoms likely replacing cerium ions. In-situ doped catalysts generally resulted in Ce^{4+} to Ce^{3+} reduction at lower temperatures and a more stable lattice at higher temperatures compared to impregnated catalysts. The degree of Ni^{2+} to Ni^0 reduction increased with temperature.

In-situ DRIFTS was used to probe the surface chemistry of an impregnated and in-situ doped catalyst. Both materials exhibited nearly identical surface chemistry, likely involving an associative pathway at lower temperatures and a redox pathway at higher temperatures.

6. Acknowledgements

The research carried out at Brookhaven National Laboratory was supported by the U.S. Department of Energy, Office of Science and Office of Basic Energy Sciences under contract No. DE-SC0012704. S.D.S is also supported by a U.S. Department of Energy Early Career Award. This research used resources of the 23-ID-2 (IOS) beamline of the National Synchrotron Light Source II, a U.S. Department of Energy (DOE) Office of Science User Facility operated for the DOE Office of Science by Brookhaven National Laboratory under Contract No. DE-SC0012704. This work also used resources of the Advanced Photon Source (17B-M and 20BM), a U.S. Department of Energy (DOE) Office of Science User Facility operated for the DOE Office of Science by Argonne National Laboratory under Contract No. DE-AC02-06CH11357. J. L. is a Serra Hunter Fellow and is grateful to the ICREA Academia Program and MINECO/FEDER grant ENE2015-63969-R. SLS acknowledges support from the U.S. Department of Energy, Office of Basic Energy Sciences, Division of Chemical, Biological and Geological Sciences (grant DE-FG02-86ER13622A00), as well as the assistance of the Bioscience Electron Microscopy Laboratory of the University of Connecticut and grant # 1126100 for the purchase of the FEI NovaSEM.

References

[1] C.J. Guild, D. Vovchok, D.A. Kriz, A. Bruix, B. Hammer, J. Llorca, W. Xu, A. El-Sawy, S. Biswas, J.A. Rodriguez, S.D. Senanayake, S.L. Suib, Water-Gas-Shift over Metal-Free Nanocrystalline Ceria: An Experimental and Theoretical Study, ChemCatChem, 9 (2017) 1373-1377.
[2] D. Vovchok, C.J. Guild, J. Llorca, W. Xu, T. Jafari, P. Toloueinia, D. Kriz, I. Waluyo, R.M. Palomino, J.A. Rodriguez, S.L. Suib, S.D. Senanayake, Cu supported on mesoporous ceria: water gas shift activity at low Cu loadings through metal-support interactions, Physical Chemistry Chemical Physics, (2017).
[3] D.S. Newsome, The Water-Gas Shift Reaction, Catalysis Reviews, 21 (1980) 275-318.
[4] S. Tada, T. Shimizu, H. Kameyama, T. Haneda, R. Kikuchi, Ni/CeO2 catalysts with high CO2 methanation activity and high CH4 selectivity at low temperatures, International Journal of Hydrogen Energy, 37 (2012) 5527-5531.
[5] S.D. Senanayake, J. Evans, S. Agnoli, L. Barrio, T.-L. Chen, J. Hrbek, J.A. Rodriguez, Water–Gas Shift and CO Methanation Reactions over Ni–CeO2(111) Catalysts, Topics in Catalysis, 54 (2011) 34-41.
[6] X. Du, D. Zhang, L. Shi, R. Gao, J. Zhang, Morphology Dependence of Catalytic Properties of Ni/CeO2 Nanostructures for Carbon Dioxide Reforming of Methane, The Journal of Physical Chemistry C, 116 (2012) 10009-10016.
[7] L. Foppa, T. Margossian, S.M. Kim, C. Müller, C. Copéret, K. Larmier, A. Comas-Vives, Contrasting the Role of Ni/Al2O3 Interfaces in Water–Gas Shift and Dry Reforming of Methane, Journal of the American Chemical Society, 139 (2017) 17128-17139.
[8] S. Hilaire, X. Wang, T. Luo, R.J. Gorte, J. Wagner, A comparative study of water-gas-shift reaction over ceria supported metallic catalysts, Applied Catalysis A: General, 215 (2001) 271-278.
[9] B. Chamnankid, K. Föttinger, G. Rupprechter, P. Kongkachuichay, Ni–CeO2–ZrO2 Catalysts for Water Gas Shift Reaction: Effect of CeO2 Contents and Reduction Temperature, Journal of Nanoscience and Nanotechnology, 16 (2016) 12904-12909.
[10] L. Bobrova, D. Andreev, E. Ivanov, N. Mezentseva, M. Simonov, L. Makarshin, A. Gribovskii, V. Sadykov, Water–Gas Shift Reaction over Ni/CeO2 Catalysts, Catalysts, 7 (2017) 310.
[11] L. Wang, H. Liu, Y. Liu, Y. Chen, S. Yang, Influence of preparation method on performance of Ni-CeO2 catalysts for reverse water-gas shift reaction, Journal of Rare Earths, 31 (2013) 559-564.
[12] E.T. Saw, U. Oemar, M.L. Ang, H. Kus, S. Kawi, High-temperature water gas shift reaction on Ni-Cu/CeO2 catalysts: effect of ceria nanocrystal size on carboxylate formation, Catalysis Science & Technology, 6 (2016) 5336-5349.
[13] M.L. Ang, U. Oemar, E.T. Saw, L. Mo, Y. Kathiraser, B.H. Chia, S. Kawi, Highly Active Ni/xNa/CeO2 Catalyst for the Water–Gas Shift Reaction: Effect of Sodium on Methane Suppression, ACS Catalysis, 4 (2014) 3237-3248.
[14] P.J. Chupas, K.W. Chapman, C. Kurtz, J.C. Hanson, P.L. Lee, C.P. Grey, A versatile sample-environment cell for non-ambient X-ray scattering experiments, Journal of Applied Crystallography, 41 (2008) 822-824.
[15] B.H. Toby, R.B. Von Dreele, GSAS-II: the genesis of a modern open-source all purpose crystallography software package, Journal of Applied Crystallography, 46 (2013) 544-549.
[16] A. Albinati, B.T.M. Willis, The Rietveld method in neutron and X-ray powder diffraction, Journal of Applied Crystallography, 15 (1982) 361-374.
[17] B. Ravel, M. Newville, ATHENA, ARTEMIS, HEPHAESTUS: data analysis for X-ray absorption spectroscopy using IFEFFIT, J Synchrotron Radiat, 12 (2005) 537-541.

[18] L.A.J. Garvie, P.R. Buseck, Determination of Ce4+/Ce3+ in electron-beam-damaged CeO2 by electron energy-loss spectroscopy, Journal of Physics and Chemistry of Solids, 60 (1999) 1943-1947.
[19] H. Wang, D.S. Patil, W. Gu, L. Jacquamet, S. Friedrich, T. Funk, S.P. Cramer, L-edge X-ray absorption spectroscopy of some Ni enzymes: probe of Ni electronic structure, Journal of Electron Spectroscopy and Related Phenomena, 114-116 (2001) 855-863.
[20] X. Wang, J.C. Hanson, J.A. Rodriguez, C. Belver, M. Fernández-García, The structural and electronic properties of nanostructured Ce1−x−yZrxTbyO2 ternary oxides: Unusual concentration of Tb3+ and metal↔oxygen↔metal interactions, The Journal of Chemical Physics, 122 (2005) 154711.
[21] J.A. Rodriguez, J.C. Hanson, J.-Y. Kim, G. Liu, A. Iglesias-Juez, M. Fernández-García, Properties of CeO2 and Ce1-xZrxO2 Nanoparticles: X-ray Absorption Near-Edge Spectroscopy, Density Functional, and Time-Resolved X-ray Diffraction Studies, The Journal of Physical Chemistry B, 107 (2003) 3535-3543.
[22] S. Kumar, S. Gautam, T.K. Song, K.H. Chae, K.W. Jang, S.S. Kim, Electronic structure study of Co doped CeO2 nanoparticles using X-ray absorption fine structure spectroscopy, Journal of Alloys and Compounds, 611 (2014) 329-334.
[23] A. Ponchel, A. D'Huysser, C. Lamonier, L. Jalowiecki-Duhamel, CeNiO and CeAlNiO solids studied by electron microscopy, XRD, XPS and depth sputtering techniques, Physical Chemistry Chemical Physics, 2 (2000) 303-312.
[24] Z. Liu, T. Duchon, H. Wang, D.C. Grinter, I. Waluyo, J. Zhou, Q. Liu, B. Jeong, E.J. Crumlin, V. Matolin, D.J. Stacchiola, J.A. Rodriguez, S.D. Senanayake, Ambient pressure XPS and IRRAS investigation of ethanol steam reforming on Ni-CeO2(111) catalysts: an in situ study of C-C and O-H bond scission, Physical Chemistry Chemical Physics, 18 (2016) 16621-16628.
[25] D. Vovchok, C.J. Guild, S. Dissanayake, J. Llorca, E. Stavitski, Z. Liu, R.M. Palomino, I. Waluyo, Y. Li, A.I. Frenkel, J.A. Rodriguez, S.L. Suib, S.D. Senanayake, In Situ Characterization of Mesoporous Co/CeO2 Catalysts for the High-Temperature Water-Gas Shift, The Journal of Physical Chemistry C, 122 (2018) 8998-9008.
[26] N. Schumacher, A. Boisen, S. Dahl, A.A. Gokhale, S. Kandoi, L.C. Grabow, J.A. Dumesic, M. Mavrikakis, I. Chorkendorff, Trends in low-temperature water–gas shift reactivity on transition metals, Journal of Catalysis, 229 (2005) 265-275.
[27] C. Javier, L.D. David, L. Zongyuan, D. Tomáš, E. Jaime, S.S. D., C.E. J., M. Vladimir, R.J. A., G.P.M. Verónica, In Situ and Theoretical Studies for the Dissociation of Water on an Active Ni/CeO2 Catalyst: Importance of Strong Metal–Support Interactions for the Cleavage of O–H Bonds, Angewandte Chemie International Edition, 54 (2015) 3917-3921.
[28] W.Q. Xu, R. Si, S.D. Senanayake, J. Llorca, H. Idriss, D. Stacchiola, J.C. Hanson, J.A. Rodriguez, In situ studies of CeO2-supported Pt, Ru, and Pt-Ru alloy catalysts for the water-gas shift reaction: Active phases and reaction intermediates, Journal of Catalysis, 291 (2012) 117-126.
[29] X. Wang, J.A. Rodriguez, J.C. Hanson, D. Gamarra, A. Martinez-Arias, M. Fernandez-Garcia, In situ studies of the active sites for the water gas shift reaction over Cu-CeO2 catalysts: complex interaction between metallic copper and oxygen vacancies of ceria, J Phys Chem B, 110 (2006) 428-434.
[30] F. Zhao, Z. Liu, W. Xu, S. Yao, A. Kubacka, A.C. Johnston-Peck, S.D. Senanayake, A.-Q. Zhang, E.A. Stach, M. Fernández-García, J.A. Rodriguez, Water-Gas Shift Reaction on Ni–W–Ce Catalysts: Catalytic Activity and Structural Characterization, The Journal of Physical Chemistry C, 118 (2014) 2528-2538.
[31] C. Binet, M. Daturi, J.C. Lavalley, IR study of polycrystalline ceria properties in oxidised and reduced states, Catalysis Today, 50 (1999) 207-225.